

Effect of SO_4^{2-} and AC Interference on Chloride-Induced Corrosion Behavior of CoCrFeMnNi High Entropy Alloy in a Simulated Concrete Pore Solution

Yanqi Zeng¹, Min Zhu¹, Jian Zhou^{1,*}, Fangming Shen², Jinjian Zhang², Mingfeng Ye³, Zhaohu Yu³

¹ School of Mechanical Engineering & Automation, Zhejiang Sci-Tech University, Hangzhou 310018, PR China

² Zhejiang Quzhou Yongzheng Lithium Technology Co., Ltd., Quzhou 324012, China

³ Changshan Chengxin bearing Co., Ltd., Changshan 324000, China

*E-mail: zmii666@126.com

Received: 5 February 2022 / Accepted: 17 March 2022 / Published: 5 April 2022

The inhibition influence of sulfate ion (SO_4^{2-}) on the corrosion of CoCrFeMnNi HEA under AC interference was studied in chloride contaminated concrete pore solution using electrochemical measurements, atomic force microscopy (AFM) and immersion test. The results show that increasing SO_4^{2-} concentration inhibits chloride-induced corrosion and AC interference degrades the compactness and protective capacity of passive film. Under AC interference, the inhibition effect of SO_4^{2-} on the corrosion of the HEA is more remarkable. A decrease in the contents of Fe, Co and Ni elements induces the generation of pits.

Keywords: High entropy alloy, Sulphate ion, AC interference, Corrosion behavior

1. INTRODUCTION

High entropy alloys (HEAs), as emergent materials, are made of mixing alloy elements with approximately equiatomic concentrations [1-3], which have four core effects: high configurational entropy, severe lattice distortion, cocktail effect and sluggish diffusion [4-6]. These effects create unique microstructure, exceptional physical and mechanical properties, including superior structural stability, good thermal stability, high strength, excellent wear and corrosion resistance [5-8]. Meanwhile, HEAs have drawn unprecedented attention for industrial applications due to many extraordinary properties [9,10]. It has been found that HEAs consist of simple solid solutions with a single phase or dual phases [11,12]. Among different HEAs, equiatomic CoCrFeMnNi HEA is one of the most typical single phase HEA, firstly developed by Cantor et al, and exhibits a stable single face-centered cubic (FCC) structure,

and numerous studies have been unveiled that CoCrFeMnNi HEA presents desirable properties [13-15]. For example, Kim [16] fabricated equiatomic CoCrFeMnNi using selective laser melting (SLM) with a high yield strength of 778.4 MPa. Zheng [17] explored the influence of different cooling rates on the microstructure evolution/mechanical property of CoCrFeMnNi HEA. And the yield strength and tensile strength increased to 428 MPa and 584 MPa at fast cooling rate. Sun [18] investigated CoCrFeMnNi HEA processed by different annealing treatments and revealed that the HEA possessed exceptional mechanical property at cryogenic temperatures. Xu [19] designed and prepared graphene encapsulated equiatomic CoCrFeMnNi micro/nanoparticles, and its hardness and compressive yield strength significantly raised to about 2.33 GP and 1350 MPa. Consequently, CoCrFeMnNi HEA as an extremely promising alloy material may replace conventional alloys in modern industrial applications.

Concrete is one of the most common building materials employed in construction projects [20-22]. The durability of concrete structures has been widely concerned in the architecture field, and corrosion failure is the main reason for the degradation of concrete structures and results in service risks and economic loss [21-25]. Hence, the high corrosion resistance of metal materials utilized in concrete structures is particularly important. Existing studies have implied that CoCrFeMnNi HEA has unexpected corrosion resistance. For instance, Luo [26] studied the corrosion behavior of CoCrFeMnNi HEA compared with 304 L stainless steel (SS) in 0.1 M H₂SO₄ solution, and the thickness of the passive film formed on the surface of the HEA was thicker than that on 304L SS. Ye [27] manufactured crack-free CrMnFeCoNi HEA coating on the A36 steel substrate by laser surface alloying and the coating provided better corrosion resistance than the matrix. Xu [28] researched the corrosion resistance of SLMed and as-cast CoCrFeMnNi HEAs in NaCl solution. The corrosion current densities (i_{corr}) of the SLMed and as-cast specimens are 0.4737 $\mu\text{A}\cdot\text{cm}^{-2}$ and 1.123 $\mu\text{A}\cdot\text{cm}^{-2}$, respectively. In addition, our previous studies [29,30] indicated that CoCrFeMnNi HEA exhibited an obvious secondary passive state. Thus, the HEA may be applied in reinforced concrete structure.

In underground construction facilities, the steel rebars in concrete structures are usually exposed to the coexistence environment of chloride and sulfate ions [31-33]. Some literature found that the addition of sulfate ion (SO_4^{2-}) could markedly influence the corrosion behavior of metals in the solutions containing chloride ions (Cl^-) and the erosion effect of chloride ion could be alleviated when SO_4^{2-} concentration in the solution reached a certain level [25,34-37]. However, the study on the inhibition mechanism of SO_4^{2-} on the corrosion of metals is inadequate. Moreover, in the service process, concrete structures may be suffered by AC interference [38]. Up to now, there is no literature on the corrosion behavior of CoCrFeMnNi HEA under the combined action of SO_4^{2-} and AC interference. Hence, it is necessary to carry out the related research. The results can provide reference for the practical application of CoCrFeMnNi HEA in concrete structures.

2. EXPERIMENTAL

2.1. Material and solution

Alloy elements with the purity of more than 99.9 wt% were melted, mixed and solidified in an induction suspension furnace under a high-purity argon atmosphere to prepare as-cast ingots. The melting temperature was risen to 1700 °C. Then, these ingots were cooled in the furnace for 30 min and

remelted more than 4 times to ensure composition homogenization. The chemical composition of the HEA was given in Table 1. Each sample with a size of 10 mm × 10 mm × 3 mm was cut from the ingot and embedded by epoxy resin, leaving an exposed working area of 1 cm². Before testing, the sample surface was ground with a series of 320-2000 grit silicon carbide (SiC) sandpapers and polished with 0.5 μm diamond grinding paste. Subsequently, the polished samples were rinsed with ultrapure water and ethanol using the ultrasonic cleaner and dried in cool air. Fig. 1 displays the microstructure of the HEA etched for 5s with aqua regia. Clearly, the HEA is mainly composed of a single phase FCC structure.

Table 1. The average chemical composition of CoCrFeMnNi HEA (wt.%).

Element	Co K	Cr K	Ni K	Mn K	Fe K
Wt.%	21.3	19.6	20.2	20.5	Bal.

In this work, 0.001 M Ca(OH)₂+0.2 M NaOH+0.6 M KOH was adopted to simulate the concrete pore solution [39,40]. 0.4 M NaCl and different Na₂SO₄ concentrations were added to prepare the test solutions with various [SO₄²⁻]/[Cl⁻] ratios of 0, 0.5, 1.0 and 1.5. The solution temperature was kept at 30 °C.

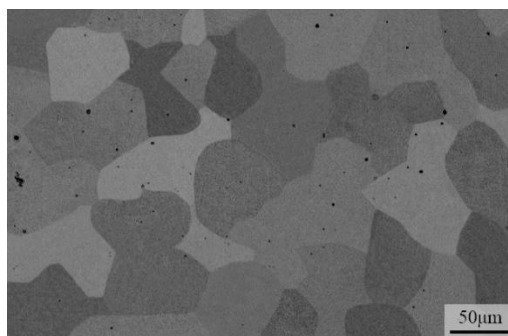


Figure 1. Microstructure of as-cast CoCrFeMnNi HEA.

2.2. Electrochemical tests

The electrochemical measurements were conducted in the above-mentioned concrete pore solutions with a CHI660E electrochemical workstation using a three-electrode cell. The HEA sample was employed as the working electrode, a platinum sheet was acted as the auxiliary electrode, and a saturated calomel electrode (SCE) was served as the reference electrode. Electrochemical testing equipment for studying alternating current (AC) corrosion of the HEA was consistent with our previous studies [41,42]. The current density (i_{AC}) of a sine wave AC signal with a frequency of 50 Hz (power frequency in China) was taken as the root mean square value and measured with a high-precision clamp

meter. Before testing, the sample was immersed in the solution for 3 h of prepassivation. Subsequently, the open circuit potential (OCP) was monitored for 1800s, followed by the electrochemical impedance spectroscopy (EIS) test from 100 kHz to 10 mHz with a fixed interference signal amplitude of 10 mV. Then, under the interference of different i_{AC} (0, 50 and 100 A·m⁻²), potentiodynamic polarization curve was tested at a scan rate of 1 mV/s in the potential range of -1.0 V ~ 0.7 V.

Prior to the Mott–Schottky measurement, the passive films were grown on the HEA surface by potentiostatic polarization at a passive potential of 0.168 V (vs. SCE) for 2 h, and then applied with different i_{AC} for 5 min. The Mott–Schottky curve test was performed with a step size of 50 mV at 1 kHz from -1 V to 0.1 V. All the tests were repeated at least four times.

2.3 AFM test

To investigate the influence of SO₄²⁻ and AC interference on the property of passive films produced on the HEA surface, the topographic characteristics of passive films were measured by atomic force microscopy (AFM, XE-100E). The films were prepared in the solutions with [SO₄²⁻]/[Cl⁻] ratios of 0.5 and 1.0 via the above-mentioned potentiostatic polarization. When AC was applied, the films were interfered by 100 A/m² for 5 min.

2.4 Immersion test

The HEA samples interfered with different i_{AC} of 0-100 A/m² were soaked in different solutions for 108 h. After test, the corroded specimens were washed, dried and weighted. The corrosion rates were obtained according to the weight loss data. The corrosion morphologies and elemental distribution of the HEA surface were analyzed by scanning electron microscope (SEM, FEI Quanta 250) equipped with an energy dispersive spectroscopy (EDS).

3. RESULTS AND DISCUSSION

3.1 Electrochemical measurements

Fig. 2 exhibits the OCP curves for the HEA in simulated concrete pore solutions with different [SO₄²⁻]/[Cl⁻] ratios. The OCP shifts positively as [SO₄²⁻]/[Cl⁻] ratio increases. The decreasing corrosion tendency indicates that the addition of sulphate ions to the chloride polluted concrete pore solution may cause an inhibited effect on the corrosion of the HEA.

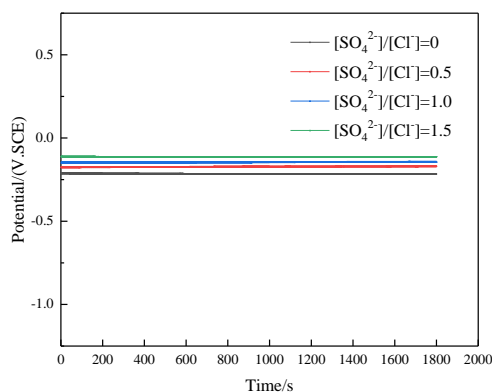


Figure 2. OCP plots for the HEA sample exposed to concrete pore solutions containing various SO_4^{2-} concentrations.

Fig. 3 exhibits the EIS curves of the HEA in the chloride polluted concrete pore solutions with various SO_4^{2-} concentrations. The Nyquist plots display an incomplete capacitive loop. Obviously, the arc diameter increases with SO_4^{2-} concentration, indicating that its corrosion resistance is improved [43-45]. As shown in Fig. 3b and c, the value of $|z|$ in the low-frequency range and the phase angle at medium frequency also present the increasing tendency. This implies that in high SO_4^{2-} concentration, a dense passive film is grown on the HEA. Furthermore, two-time constants are found for all curves. The high-frequency and low-frequency time constants are related to the passive film on the HEA and the charge transfer process occurred on the electrode/solution interface, respectively.

Considering the characteristics of the EIS plots, the equivalent electrical circuit (EEC) in Fig. 4 was employed to analyze the curves. In the EEC, R_s denotes the solution resistance, R_{ct} and Q_{dl} refer to the charge transfer resistance and non-ideal electric double-layer capacitance, R_f and Q_f represent the resistance and capacitance of the passive film. The fitted R_f and R_{ct} are displayed in Fig. 5. A sharp increase in R_f and R_{ct} with the increase of SO_4^{2-} concentration is exhibited. This indicates that a compact passive film is formed on the HEA surface, which improves its corrosion resistance. This law may be due to that the addition of SO_4^{2-} decreases the damage influence of corrosive Cl^- on the passive film. As SO_4^{2-} concentration increases, the competitive adsorption between SO_4^{2-} and Cl^- causes less Cl^- to adsorb on the film surface, thus promoting the corrosion resistance of the HEA.

Fig. 6 shows the potentiodynamic polarization curves of the HEA under different i_{AC} in chloride polluted concrete pore solutions with various SO_4^{2-} concentrations. All curves exhibit an apparent passive region. The anodic current density decreases with an increasing $[\text{SO}_4^{2-}]/[\text{Cl}^-]$ ratio, which suggests that the corrosion of the HEA is remarkably inhibited by the addition of SO_4^{2-} into the concrete pore solution. Moreover, the curves measured at various $[\text{SO}_4^{2-}]/[\text{Cl}^-]$ ratios shift to the right as i_{AC} increases. This implies that AC application has an acceleration influence on the electrochemical corrosion of the HEA [30]. As shown in Fig. 7, the variation tendency of passive current density (i_p) verifies the influence of SO_4^{2-} and imposed AC. Under AC application, a great decrease in i_p implies that the inhibition influence of increasing SO_4^{2-} concentration on the corrosion of the HEA is more significant.

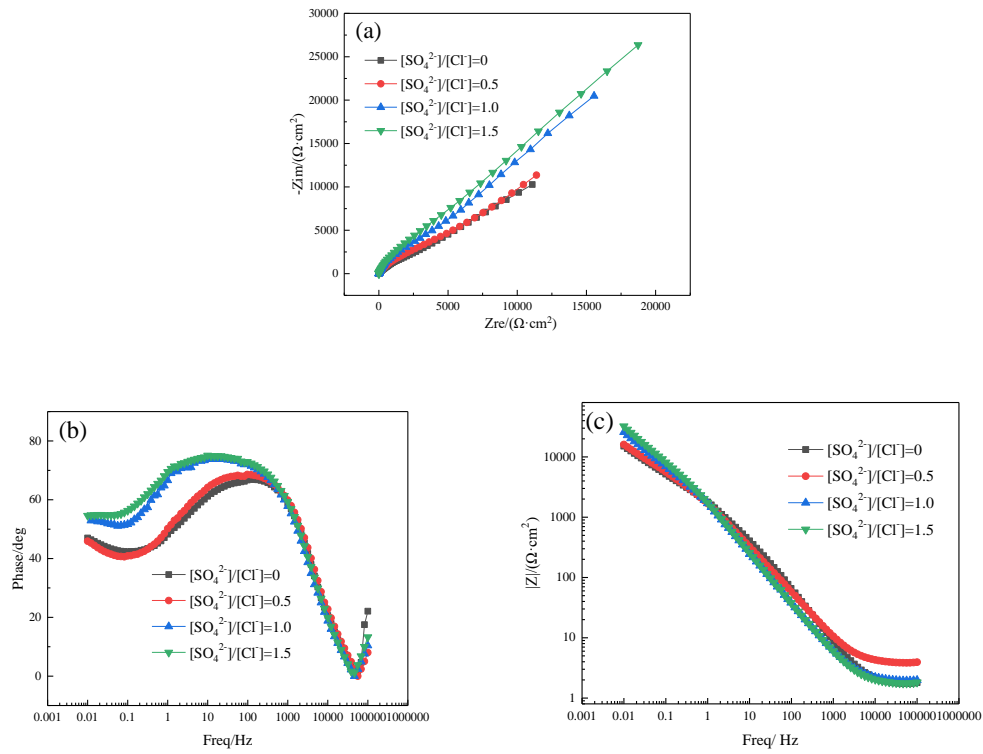


Figure 3. EIS plots for the HEA in concrete pore solutions with different SO_4^{2-} concentrations: (a) Nyquist plot (b, c) Bode plots.

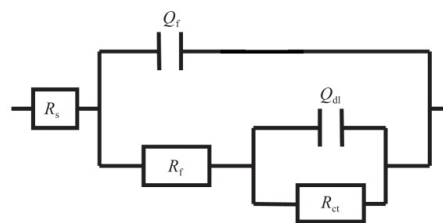


Figure 4. Equivalent electrical circuit for fitting EIS data.

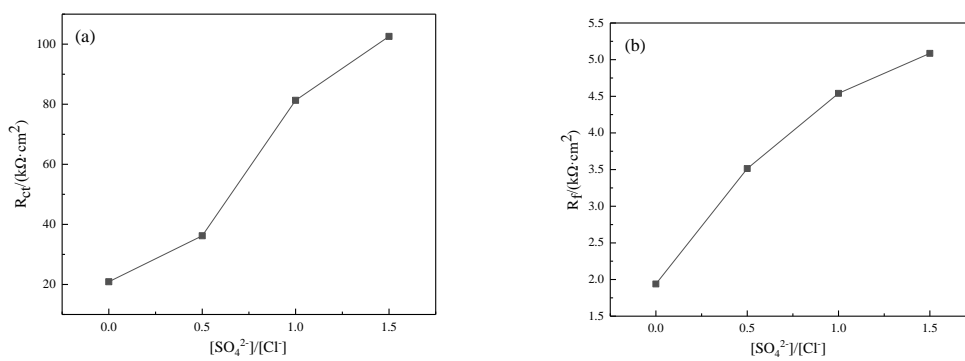


Figure 5. The variation of R_{ct} and R_f as a function of SO_4^{2-} concentrations: (a) R_{ct} ; (b) R_f .

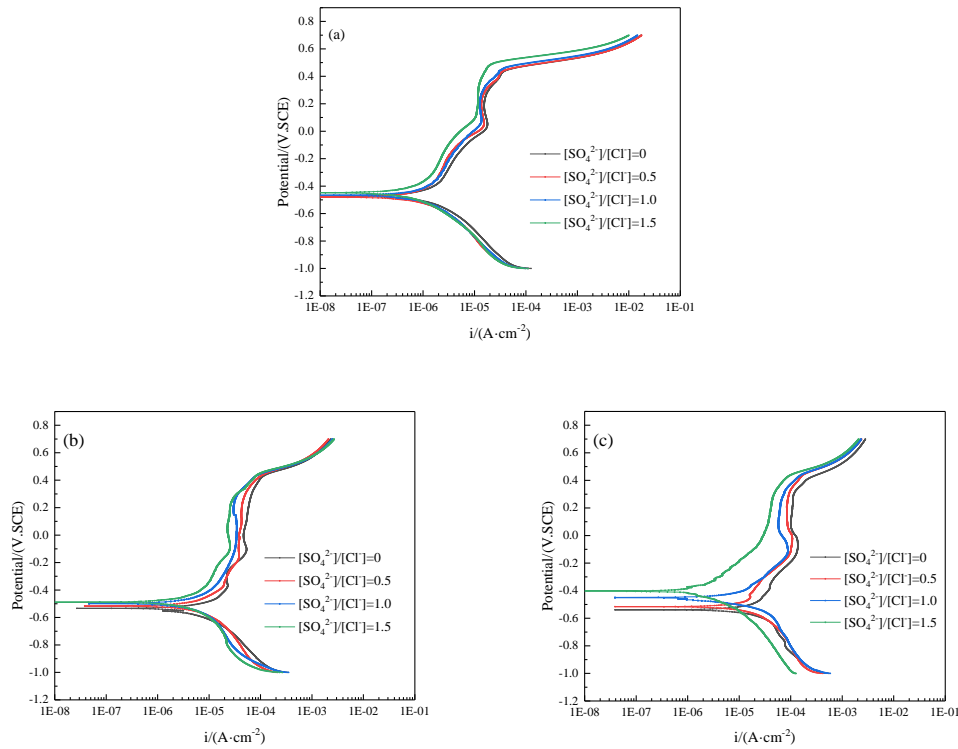


Figure 6. Potentiodynamic polarization curves of the HEA under different i_{AC} in concrete pore solutions with various SO_4^{2-} concentrations: (a) 0 A/m²; (b) 50 A/m²; (c) 100 A/m².

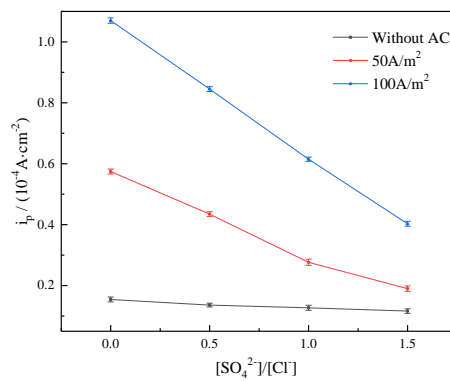


Figure 7. The values of i_p for the HEA under different i_{AC} and $[SO_4^{2-}]/[Cl^-]$ ratio.

Known from the above results, SO_4^{2-} plays an inhibition role in the chloride-induced corrosion. The possible reasons are as follows: some metal ions within the passive film react with chloride ions and produce soluble metal chlorides (MCl_x), resulting in the damage of the film. According to existing studies, when the sulphate ion is added to the solution containing chloride ions, sulfate (such as $Cr_2(SO_4)_3$) is produced within the passive film on the surface of the HEA, which reduces the solubility of the passive film and improves the stability of the surface passive film [46]. In addition, sulfate ion and chloride ion have similar ionic mobility [34], and there is a competitive adsorption relationship between the two ions, hence the presence of SO_4^{2-} decreases the adsorption of Cl^- . Moreover, SO_4^{2-} and

Ca(OH)₂ react to form an insoluble salt of CaSO₄, and then the CaSO₄ rapidly covers both anodic and cathodic reactive sites so that the corrosion reaction is hindered. Furthermore, our recent research [30,47] and Xu [48] summarized that the applied AC enhanced the electrochemical activity and diffusion rate of ions. Therefore, AC interference exerts an acceleration effect on the electrochemical corrosion of the HEA.

3.2 Mott–Schottky curve

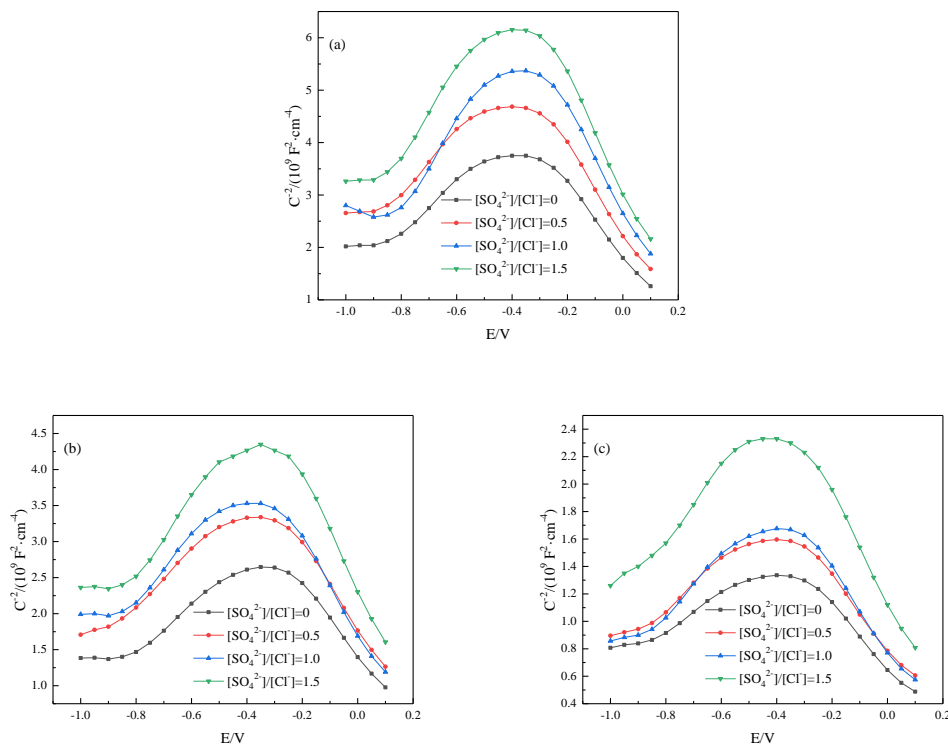


Figure 8. Mott-Schottky plots of passive films on the HEA under various i_{AC} in concrete pore solutions with different SO_4^{2-} concentrations: (a) 0 A/m²; (b) 50 A/m²; (c) 100 A/m².

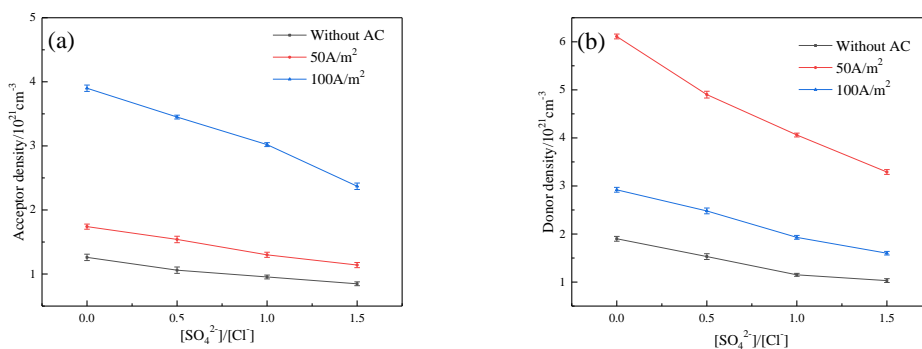


Figure 9. The calculated charge carrier densities derived from Mott-Schottky plots: (a) N_A ; (b) N_D .

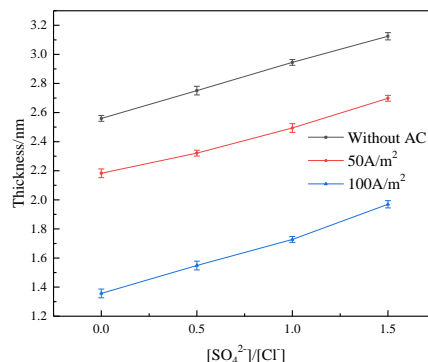


Figure 10. The values of thickness of the film under different conditions.

To deeply study the influence of SO_4^{2-} and AC interference on the semiconductor behavior of passive film produced on the surface of the HEA sample in chloride polluted concrete pore solution, Mott-Schottky curves were measured. The formula relating the space charge capacitance (C) and the external electrode potential (E) can be given as follows [49-51]:

$$\frac{1}{C^2} = \pm \frac{2}{\varepsilon \varepsilon_0 e N_D} \left(E - E_{FB} - \frac{kT}{e} \right) \quad (1)$$

Where the “ \pm ” signs represent n and p type semiconductors respectively. ε_0 is the vacuum permittivity ($8.854 \times 10^{-14} \text{ F} \cdot \text{cm}^{-1}$), ε denotes the relative dielectric constant of the passive film, in this text, $\varepsilon = 12$ [30,47,52]; e is the electron charge ($1.602 \times 10^{-19} \text{ C}$), N_D and N_A (cm^{-3}) are defined as the donor and acceptor defect densities respectively. E_{FB} represents the flat-band potential (V), K is the Boltzmann constant ($1.38 \times 10^{-23} \text{ J} \cdot \text{K}^{-1}$) and T is the absolute temperature (K). E is the applied electrode potential (V). N_A and N_D were calculated by the following formula:

$$N = \frac{2}{em\varepsilon\varepsilon_0} \quad (2)$$

where m denotes the slopes of linear portions in the curves. To further understand the difference in the anti-corrosion resistance of the HEA tested at various conditions, the passive film thickness should be considered. The thickness of passive film (d) was obtained by the following formula [51,53-56]:

$$d = \left[\frac{2\varepsilon\varepsilon_0(E - E_{FB} - kT)/e}{eN_d} \right]^{1/2} \quad (3)$$

Fig. 8 depicts the Mott-Schottky curves of passive films on the HEA applied with various AC current densities in concrete pore solutions with various SO_4^{2-} concentrations. Two linear segments are found in the curves with the positive and negative slopes, which is an indication that the passive films possess n-p type semiconducting property. This is in accord with some previous studies about the HEAs [26,29,30]. According to the existing literature on CoCrFeMnNi HEA investigated in alkaline environments, it is found that $\text{Cr}_2\text{O}_3/\text{Cr}(\text{OH})_3$ and $\text{Fe}_2\text{O}_3/\text{Fe}(\text{OH})_3$ are the main compositions of passive film formed on HEA surface [26,29,30], which exhibits p-type and n-type semiconductor characteristics, respectively [57,58]. The slopes of the linear segments of the curves increase with increasing SO_4^{2-} concentration, which implies a decrease in N_A and N_D within the passive films, as shown in Fig. 9. As SO_4^{2-} concentration increases, fewer defects are generated in the passive film, hence the paths for ions to penetrate into the substrate decrease, thus improving the resistance to local corrosion. The variation

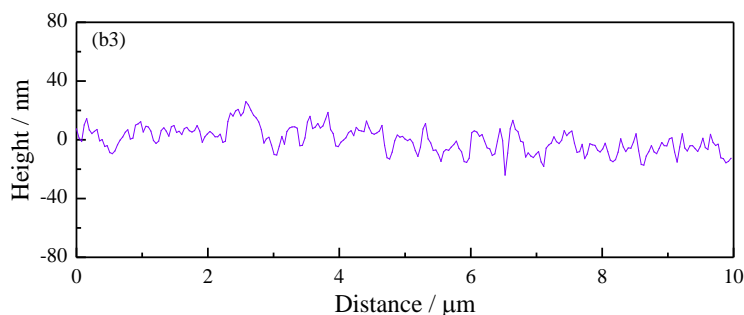
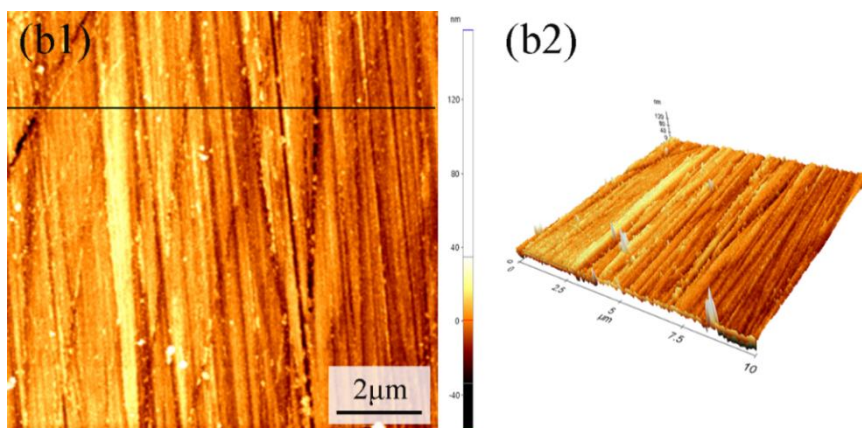
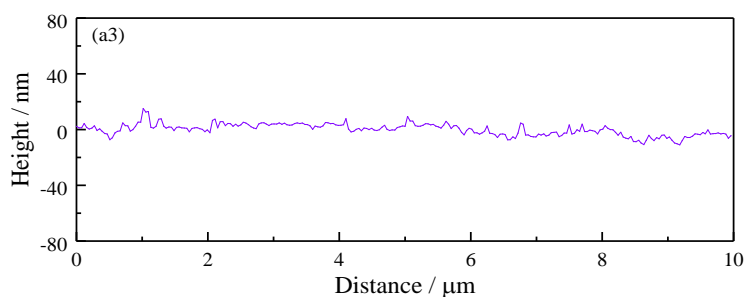
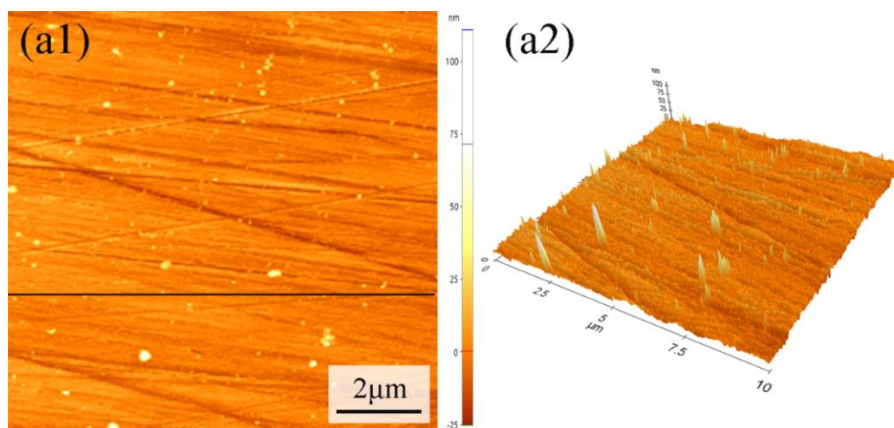
of the thickness of the films is presented in Fig. 10. The film thickness increases with increasing SO_4^{2-} concentration, indicating that SO_4^{2-} improves the protective performance of the passive film. Point defect model (PDM) can clarify the above phenomenon [59]. The n-type semiconductor is mainly composed of oxygen vacancies (V_{O}) and metal interstitials ($M_i^{\times+}$), and the p-type semiconductor includes cation vacancies ($V_m^{\times'}$). Positive and negative charges are injected at the metal/film or film/solution interfaces. These defects govern the transportation of cations from the metal substrate to the film and the penetration of anions from the solution to the film [60]. When the passive film is in solution containing Cl^- , oxygen vacancies and Cl^- react to generate new $V_{\text{O}}/V_m^{\times'}$, and the newly generated V_{O} continuously reacts with other chloride ions to produce more $V_m^{\times'}$. The $V_m^{\times'}$ can accumulate in some areas between the matrix and passive film, and hinder the growth of the film, thus breaking the dynamic balance of growth/dissolution of the stable passive film. After SO_4^{2-} is added to the solution, the contents of adsorbed chloride ions relatively decrease due to the competitive adsorption, which reduces the probability of collision and contact between the film and chloride ions, thus obstructing these reactions and reducing the formation of $V_m^{\times'}$. The existence of SO_4^{2-} hinders the aggregation of $V_m^{\times'}$, which is beneficial to promoting the stability of passive film. The defect density is proportional to the conductivity of the passive film, so a lower defect density implies a lower rate of electrochemical reaction at the solution/metal interface, thus the transportation of anions slows down, and fewer Cl^- ions occupy these vacancies inside the film. Consequently, SO_4^{2-} reduces the chemical binding ability of chloride ion and makes the internal structure of passive film to be more uniform, which can effectively repel the absorption of Cl^- on the passive film surface. This trend is more obvious with the increase of SO_4^{2-} concentration.

In addition, under various SO_4^{2-} concentrations, the values of N_A and N_D generally increase with i_{AC} , which indicates that the imposed AC damages the compactness and integrality of passive film. The broken film provides more transfer channels for ions to permeate the bare substrate, which enhances the migration efficiency of ions. Moreover, the bare matrix and residual film form micro-galvanic cells, which accelerates the anodic dissolution of CoCrFeMnNi HEA and induces the pitting initiation. By comparing with the data, the remediation effect of SO_4^{2-} on the passive film of the HEA under AC interference is more remarkable. The change trend of the film thickness in Fig. 10 manifests this. Hence, a significant inhibition effect of SO_4^{2-} on the corrosion of the HEA is exhibited.

3.3 AFM analysis

The surface topography characteristics of the passive films tested under different conditions were analyzed by AFM measurement. In Fig. 11, the surface film formed at $[\text{SO}_4^{2-}]/[\text{Cl}^-]$ ratio of 0.5 is relatively smooth, uniform and compact, with a low height undulation of 15nm. When AC is imposed, the passive film becomes uneven. As displayed in Fig. 11b3, the fluctuation range is greatly increased. Compared with Fig. 11b, the film on the HEA surface (Fig. 11c) becomes denser due to increasing SO_4^{2-} concentration. This indicates that the addition of sulfate ion reduces the rupture possibility of passive film and prevents the initiation of corrosion. In Fig. 12, the surface roughness values (R_a) of the samples with passive films under different conditions are 3.209, 5.726 and 3.705 nm, respectively. For rough

surface, chloride ion can be easily absorbed. Pradhan [61] reported that the penetration depth of corrosion solution increased with the value of R_a and the electron release rate was higher for the rougher surface. Thus, as AC current density increases, the passive film is severely damaged and the corrosion of the HEA is more obvious. Thus, the competitive absorption of SO_4^{2-} and Cl^- , as well as AC interference can affect the integrity and compactness of passive film.



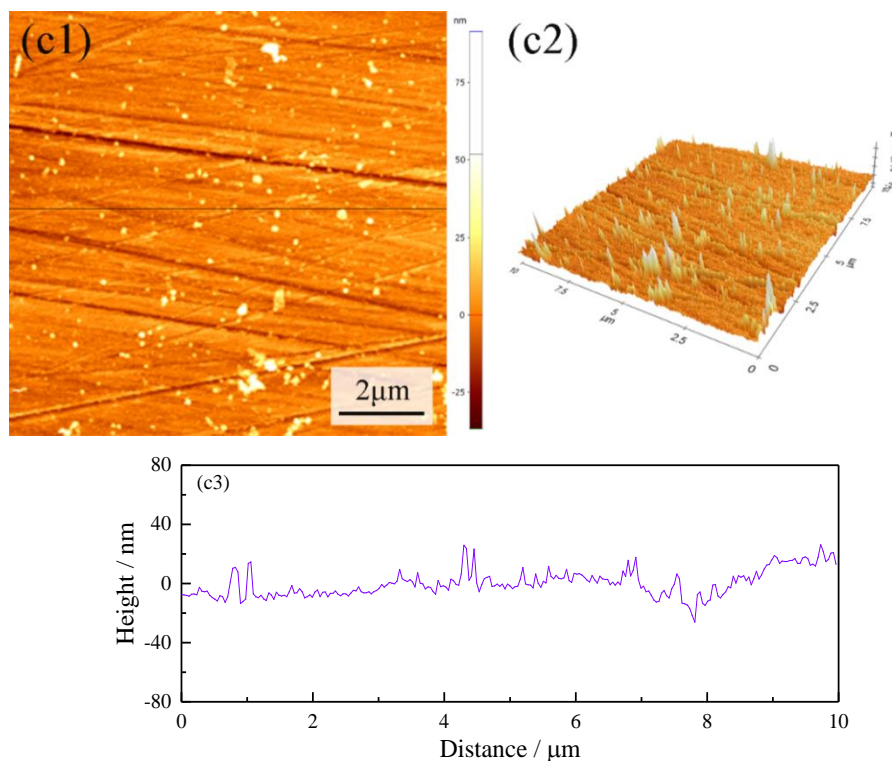


Figure 11. The topography characteristics of specimens under various conditions: (a1, b1 and c1) $[\text{SO}_4^{2-}]/[\text{Cl}^-]$ ratio of 0.5 and without AC; (a2, b2 and c2) $[\text{SO}_4^{2-}]/[\text{Cl}^-]$ ratio of 0.5 and applied i_{AC} of 100 A/m^2 ; (a3, b3, and c3) $[\text{SO}_4^{2-}]/[\text{Cl}^-]$ ratio of 1.0 and applied i_{AC} of 100 A/m^2 .

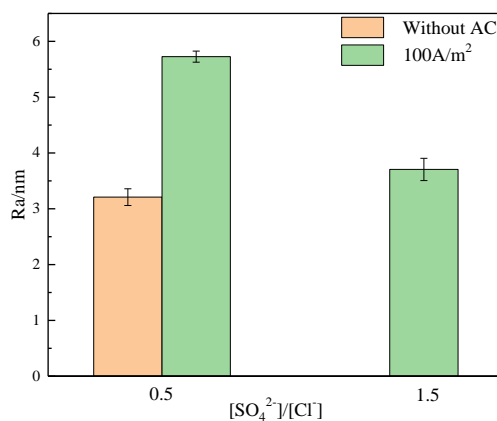


Figure 12. Roughness of specimens under various testing conditions.

3.4. Immersion test

Fig. 13 exhibits the comparison of corrosion rates of CoCrFeMnNi HEA under various conditions. At 50 A/m^2 , the corrosion rate of the HEA gradually reduces with increasing concentration of sulphate ion, which implies that the anti-corrosion resistance of the HEA is significantly improved with increasing sulphate ion. When the $[\text{SO}_4^{2-}]/[\text{Cl}^-]$ ratio is 0.5, the corrosion rate increases by 1.68

times from i_{AC} of 50 A/m^2 to 100 A/m^2 , which means that AC application induces the occurrence of severe corrosion. To illuminate the effects of SO_4^{2-} and AC interference on the corrosion behavior of the HEA, the surface corrosion morphologies are observed and shown in Fig. 14 (a)–(h). The corrosion morphologies of the HEA tested under various conditions present the characteristics of localized corrosion, but there is a significant difference in the corrosion degree. When the $[\text{SO}_4^{2-}]/[\text{Cl}^-]$ ratio is 0.5 and i_{AC} is 50 A/m^2 , as seen in Fig.14(a) and (b), many pits with different sizes are distributed on the HEA sample, and some part of pits dissolve together. Thus, the corrosion status under this condition is relatively serious. As $[\text{SO}_4^{2-}]/[\text{Cl}^-]$ ratio rises, the number and size of pitting gradually decrease. Especially for $[\text{SO}_4^{2-}]/[\text{Cl}^-]$ ratio of 1.5, only few small pits are sporadically generated on the HEA surface. The slightest corrosion degree demonstrates that increasing SO_4^{2-} concentration significantly improves the anti-corrosion property of the HEA. However, under the conditions of $[\text{SO}_4^{2-}]/[\text{Cl}^-]$ ratio of 0.5 and the i_{AC} of 100 A/m^2 , compared with that exhibited in Fig. 14(a) and (b), the severe corrosion characteristics with more pits reveal that increasing i_{AC} promotes the corrosion of the HEA. Furthermore, the morphologies and point scanning EDS results of pits on the HEA tested under various conditions are displayed in Fig. 15. The point 1 denotes the FCC matrix and the point 2 represents the interior of pitting. By comparing the data, it can be concluded that the formation of pitting is due to the decrease of the contents of Fe, Co, and Ni elements. The EDS mapping presented in Fig. 16 also verifies this. Moreover, the variation of surface corrosion morphology in Fig.15 confirms the influences of SO_4^{2-} and AC interference on the corrosion of the HEA.

As has been reported in the literature [52], the anti-corrosion resistance of the HEA was enhanced in a chlorinated concrete solution, which may be related to the change in the microstructure.

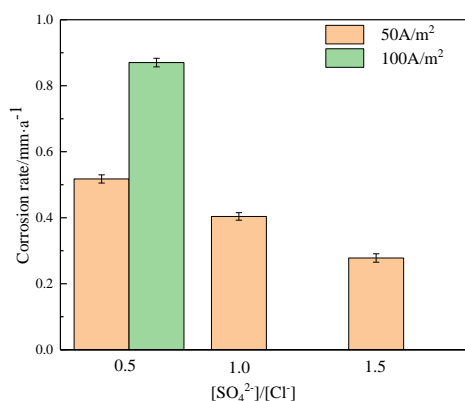
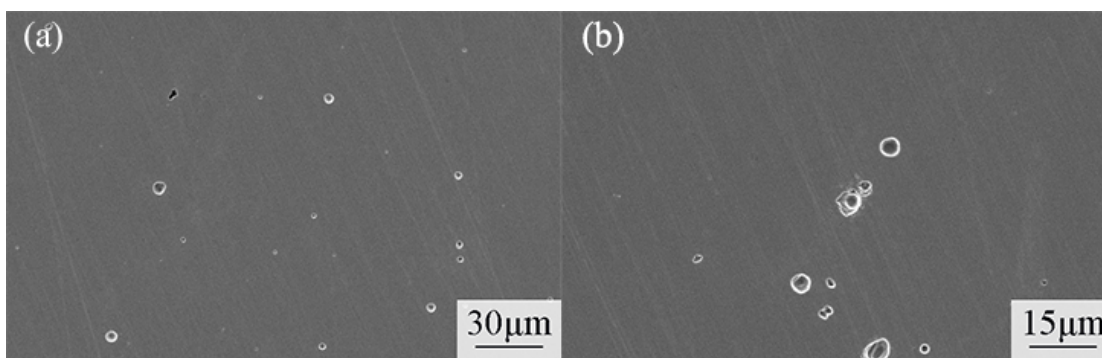


Figure 13. Corrosion rates of CoCrFeMnNi HEA immersed at different conditions for 108h.



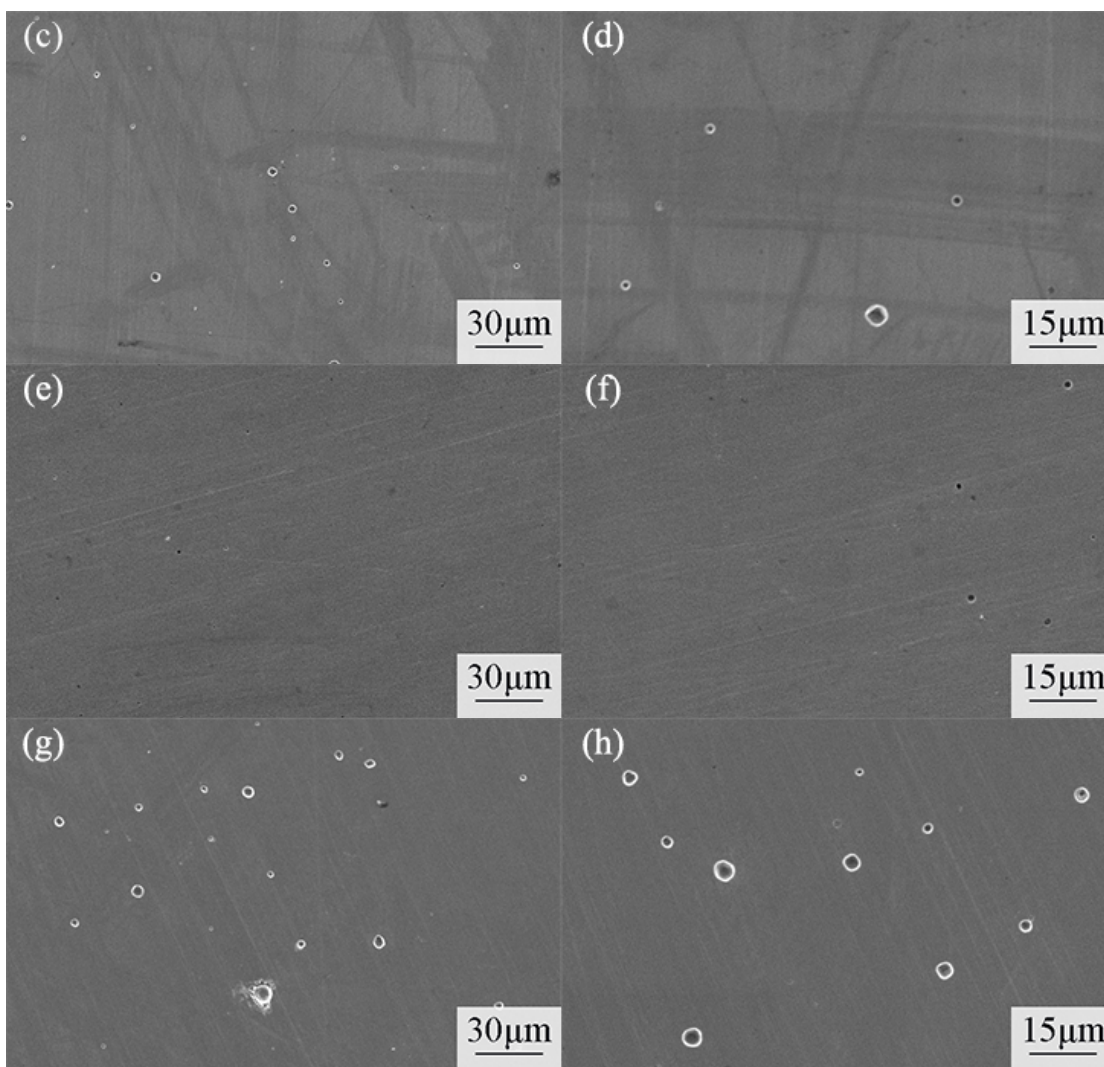
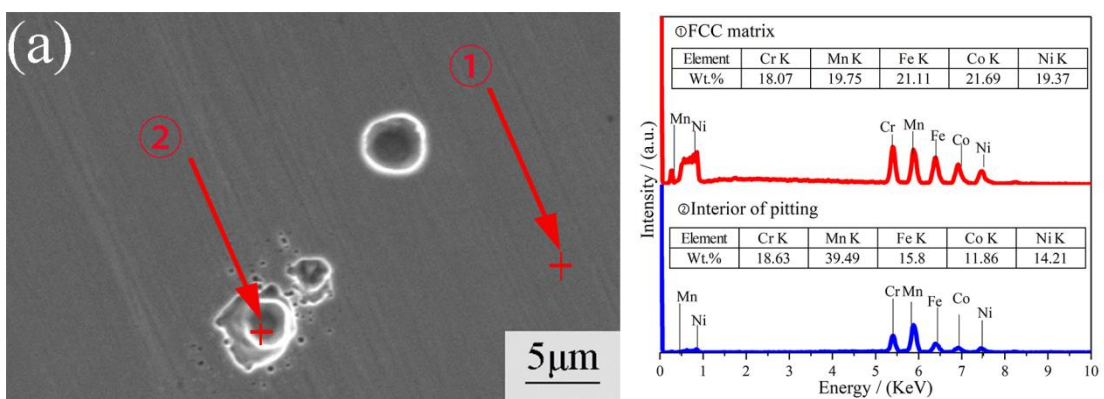


Figure 14. Corrosion morphologies of the HEA immersed under different conditions for 108h: (a, b) $[SO_4^{2-}]/[Cl^-]$ ratio of 0.5 and i_{AC} of $50 A/m^2$; (c, d) $[SO_4^{2-}]/[Cl^-]$ ratio of 1.0 and i_{AC} of $50 A/m^2$; (e, f) $[SO_4^{2-}]/[Cl^-]$ ratio of 1.5 and i_{AC} of $50 A/m^2$; (g, h) $[SO_4^{2-}]/[Cl^-]$ ratio of 0.5 and i_{AC} of $100 A/m^2$.



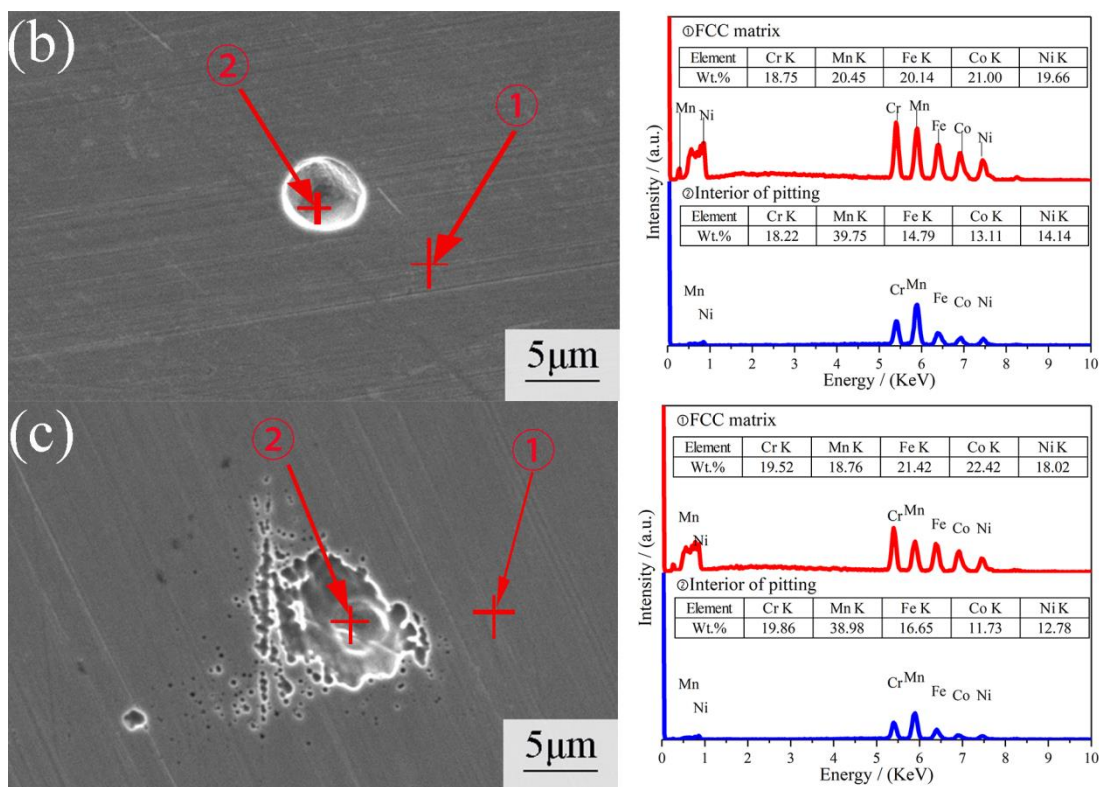


Figure 15. Surface corrosion morphologies and EDS point-scanning results of HEA under various conditions: (a) $[SO_4^{2-}]/[Cl^-]$ ratio of 0.5 and i_{AC} of 50 A/m²; (b) $[SO_4^{2-}]/[Cl^-]$ ratio of 1.0 and i_{AC} of 50 A/m²; (c) $[SO_4^{2-}]/[Cl^-]$ ratio of 0.5 and i_{AC} of 100 A/m².

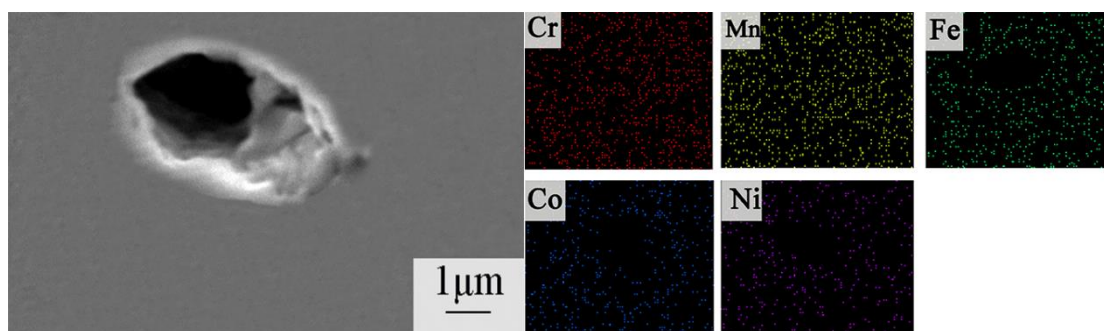


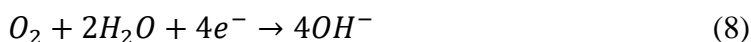
Figure 16. EDS mapping of HEA sample interfered at i_{AC} of 100 A/m² in concrete pore solution with $[SO_4^{2-}]/[Cl^-]$ ratio of 0.5.

According to the above EDS results and previous literature [52], the possible anode and cathode reactions are as follows:

Anode reactions:



Cathode reaction:



4. CONCLUSIONS

In this paper, the influence of sulphate ion and AC interference on the corrosion behavior of CoCrFeMnNi HEA was systematically studied. The main conclusions are as follows:

- 1) With the increase of i_{AC} , the protection of passive film weakens, and more severe local corrosion occurs on the HEA surface.
- 2) Increasing SO_4^{2-} concentration significantly improves the anti-corrosion property of the HEA. The inhibition effect of sulfate ion on the corrosion of the HEA is more significant under AC interference.
- 3) A decrease in the contents of Fe, Co and Ni elements induces the generation of pits.

ACKNOWLEDGEMENTS

This work was supported by the National Natural Science Foundation of China (No. 51871026) and National Material Environmental Corrosion Infrastructure.

References

1. M.Z. Wang, Z.Q. Wen, B. Ma, J.X. Liu, Z.G. Zou and Y.H. Zhao, *J. Alloy. Compd.*, 893(2022)162242.
2. S. Yadav, Q.F. Zhang, A. Behera, R.S. Haridas, P. Agrawal, J.D. Gong and R.S. Mishra, *J. Alloy. Compd.*, 877(2021)160265.
3. H.W. Lan and Q.B. Liu, *Intermetallics*, 126(2020)106941.
4. Y.F. Ye, Q. Wang, J. Lu, C.T. Liu and Y. Yang, *Mater. Today.*, 19(2016)349.
5. B.C. Ocak and G. Goller, *J. Eur. Ceram. Soc.*, 41(2021)6290.
6. O.N. Senkov, S.V. Senkova, C. Woodward and D.B. Miracle, *Acta Mater.*, 61(2013)1545.
7. J. Yang, F.F. Zhang, Q.S. Chen, W. Zhang, C. D. Zhu, J.G. Deng, Y.L. Zhong, J.L. Liao, Y.Y. Yang, N. Liu and J.J. Yang, *Corros. Sci.*, 192(2021)109862.
8. R. Li, Y.M. Ma, X.S. Liu, Y. Lu, Y.F. Zhang, P.F. Yu and G. Li, *Intermetallics*, 140(2022)107388.
9. P. Moazzen, M.R. Toroghinejad, T. Zargar and P. Cavaliere, *J. Alloy. Compd.*, 892(2021)161924.
10. S. Yang, J. Lu, F.Z. Xing, L.J. Zhang and Y. Zhong, *Acta Mater.*, 192(2020)11.
11. P. Thirathipviwat, Y. Onuki, G. Song, J. Han and S. Sato, *J. Alloy. Compd.*, 890(2022)161816.
12. T.H. Yang, B. Cai, Y.J. Shi, M.X. Wang and G.P. Zhang, *Micron*, 147(2021)103082.
13. X.L. Ren, B.D. Yao, T. Zhu, Z.H. Zhong, Y.X. Wang, X.Z. Cao, S. Jinno and Q. Xu, *Intermetallics*, 126(2020) 106942.
14. Y.M. Qi, T.W. He, H.M. Xu, Y.D. Hu, M. Wang and M.L. Feng, *J. Alloy. Compd.*, 871(2021)159516.
15. Y.M. Qi, M. Zhao and M.L. Feng, *J. Alloy. Compd.*, 851(2021)156923.
16. Y.K. Kim, J. Choe and K.A. Lee, *J. Alloy. Compd.*, 805(2019)680.
17. H.T. Zheng, Qi. Xu, R.R. Chen, G. Qin, XZ. Li, Y.Q. Su, J.J. Guo and H.Z. Fu, *Intermetallics*, 119(2020) 106723.
18. S.J. Sun, Y.Z. Tian, H.R. Lin, X.G. Dong, Y.H. Wang, Z.J. Wang and Z.F. Zhang, *J. Alloy.*

- Compd.*, 806(2019) 992.
19. H.Q. Xu, J.B. Zang, Y.G. Yuan, Y.K. Zhou, P.F. Tian and Y.H. Wan, *J. Alloy. Compd.*, 811(2019)152082.
 20. T. Bansal, V. Talakokula and K. Mathiyazhagan, *Measurement*, 187(2022)110202.
 21. M. Siahkouhi, G. Razaqpur, N.A. Hoult, M.H. Baghban and G.Q. Jing, *Constr. Build. Mater.*, 309(2021) 125137.
 22. H. Yang, C.S. Xiong, X.Y. Liu, A. Liu, T. Y. Li, R. Ding, S.P. Shah and W.H. Li, *Constr. Build. Mater.*, 307(2021)124991.
 23. P.S. Mangat, O.O. Ojedokun and P. Lambert, *Cem. Concr. Compos.*, 115(2021)103823.
 24. H.A.F. Dehwah, M. Maslehuddin and S.A. Austin, *Cem. Concr. Compos.*, 24(2002)17.
 25. X.X. Wang, J.P. Liu, Z.Q. Jin, F.X. Chen, P.H. Zhong and L. Zhang, *Cem. Concr. Compos.*, 19(2021)104314.
 26. H. Luo, Z.M. Li, A. M. Mingers and D. Raabe, *Corros. Sci.*, 134 (2018)131.
 27. Q.F. Ye, K. Feng, Z.G. Li, F.G. Lu, R.F. Li, J. Huang and Y.X. Wu, *Appl. Surf. Sci.*, 396(2017)1420.
 28. Z.L. Xu, H. Zhang, X.J. Du, Y.Z. He, H. Luo, G.S. Song, L. Mao, T.W. Zhou and L.L. Wang, *Corros. Sci.*, 177(2020)108954.
 29. M. Zhu, Q. Zhang, B.Z. Zhao, Y.F. Yuan and S.Y. Guo, *J. Mater. Eng. Perform.*, 30 (2021)918.
 30. M. Zhu, B.Z. Zhao, Y.F. Yuan, S.Y. Guo and G.Y. Wei, *J. Electroanal. Chem.*, 882 (2021)115026.
 31. F. Shaheen and B. Pradhan, *Constr. Build. Mater.*, 101(2015)99.
 32. J.K. Das and B. Pradhan, *Mater. Today: Proceedings*, 32(2020)803.
 33. J.M. Du, Z.Y. Tang, G. Li, H. Yang and L.L. Li, *Constr. Build. Mater.*, 225(2019)611.
 34. Y.L. Chou, Y.C. Wang, J.W. Yeh and H.C. Shih, *Corros. Sci.*, 52(2010)3481.
 35. H.F. Sun, C. Jiang, K. Cao, D. Yu, W. Liu, X.G. Zhang, F. Xing and D.D. Zhao, *Constr. Build. Mater.*, 302(2021)124345.
 36. F. Shaheen and B. Pradhan, *Cem. Concr. Res.*, 91(2017)73.
 37. R. Liu, L.H. Jiang, G.H. Huang, Y.R. Zhu, X.R. Liu, H.Q. Chu and C.S. Xiong, *Constr. Build. Mater.*, 113(2016)90.
 38. P.G. Wu, X.J. Zhu, L.J. Xu, W.S. Peng and G.C. Zhao, *Electrochem. Commun.*, 118(2020)106793.
 39. H.X. Qiao and B.R. Zhu, *J. Mater. Sci. Eng.*, 37(2019)107.
 40. P. Ghods, O.B. Isgor, G.A. McRae and G.P. Gub, *Corros. Sci.*, 52(2010)1649.
 41. M. Zhu, C.W. Du, X.G. Li, Z.Y. Liu, H. Li and D.W. Zhang, *Corros. Sci.*, 87(2014)224.
 42. M. Zhu, C.W. Du, X.G. Li, Z.Y. Liu, S.R. Wang, J.K. Li and D.W. Zhang, *Electrochim. Acta*, 117(2014)351.
 43. Z.W. Guo, X.R. Hui, Q.Y. Zhao, N. Guo, Y.S. Yin and T. Liu, *Corros. Sci.*, 190(2021)109687.
 44. L.A. Chen, Y.S. Lu, Y.T. Lin and Y.L. Lee, *Appl. Surf. Sci.*, 562(2021)150200.
 45. Z. Wang, Z. Feng, X.H. Fan and L. Zhang, *Corros. Sci.*, 179(2021)109146.
 46. L.B. Niu and K. Nakada, *Corros. Sci.*, 96(2015)171.
 47. M. Zhu, Q. Zhang, Y. F. Yuan, S.Y. Guo and Y.Z. Huang, *J. Electroanal. Chem.*, 864(2020)114072.
 48. L.Y. Xu, X. Su, Z.X. Yin, Y.H. Tang and Y.F. Cheng, *Corros. Sci.*, 61(2012)215.
 49. N. P. Wasekar, N. Hebalkar, A. Jyothirmayi, B. Lavakumar, M. Ramakrishna and G. Sundararajan, *Corros. Sci.*, 160(2020)108409.
 50. A.M. Oje, A.A. Ogwu, S.Ur. Rahman, A.I. Oje and N. Tsendzughul, *Corros. Sci.*, 154(2019)28.
 51. M.Q. Wang, Z.H. Zhou, Q.J. Wang, Z.H. Wang, X. Zhang and Y.Y. Liu, *J. Alloy. Compd.*, 811(2019)151962.
 52. H. Luo, S.W. Zou, Y.H. Chen, Z.M. Li, C.W. Du and X.G. Li, *Corros. Sci.*, 163(2020)108287.
 53. L. Fan, X.G. Li, C.W. Du and Z.Y. Liu, *J. Chin. Soc. Corros. Prot.*, 32(2012)322.
 54. Y. Wang, J.S. Jin, M. Zhang, F.M. Liu, X.Y. Wang, P. Gong and X.F. Tang, *J. Alloy. Compd.*, 10(2021) 161822.
 55. S. Ningshen, M.U. Kamachi, V.K. Mittal and H.S. Khatak, *Corros. Sci.*, 49(2007)481.
 56. Q. Li, X.J. Xia, Z.B. Pei, X.Q. Cheng, D.W. Zhang, K. Xiao, J. Wu and X.G. Li, *npj Mater.*

- Degrad.*, 6(2022)1.
57. J.L. Lv and H.Y. Luo, *Appl. Surf. Sci.*, 280(2013)124.
58. J.Z. Yao, D.D. Macdonald and C.F. Dong, *Corros. Sci.*, 146(2019)221.
59. A. Fattah-alhosseini, F. Soltani, F.S. hirsalimi, B. Ezadi and N. Attarzadeh, *Corros. Sci.*, 53(2011)3186.
60. J.L. Lv and H.Y. Luo, *Appl. Surf. Sci.*, 263(2012)29.
61. D. Pradhan, G.S. Mahobia, K. Chattopadhyay and V. Singh, *J. Alloy. Compd.*, 740(2018)250.

© 2022 The Authors. Published by ESG (www.electrochemsci.org). This article is an open access article distributed under the terms and conditions of the Creative Commons Attribution license (<http://creativecommons.org/licenses/by/4.0/>).